

LETTER TO THE EDITOR

# On Preferred Axes in WMAP Cosmic Microwave Background Data after Subtraction of the Integrated Sachs-Wolfe Effect

A. Rassat<sup>1,2</sup> \* and J.-L. Starck<sup>2</sup>

<sup>1</sup> Laboratoire d'Astrophysique, Ecole Polytechnique Fédérale de Lausanne (EPFL), Observatoire de Sauverny, CH-1290, Versoix, Switzerland.

<sup>2</sup> Laboratoire AIM, UMR CEA-CNRS-Paris 7, Irfu, SAp/SEDI, Service d'Astrophysique, CEA Saclay, F-91191 GIF-SUR-YVETTE CEDEX, France.

Preprint online version: May 17, 2022

## ABSTRACT

There is currently a debate over the existence of claimed statistical anomalies in the Cosmic Microwave Background (CMB). Recent work has focussed on methods for measuring statistical significance, as well as on masks and secondary anisotropies as potential causes of the anomalies. Following Rassat, Starck & Dupé 2013, we investigate simultaneously the impacts of the method used to account for masked regions and of the integrated Sachs-Wolfe (ISW) effect. We search for trends in CMB data from different years and with different masks treatment, including the latest WMAP9 data. We reconstruct the ISW field due to 2 Micron All-Sky Survey (2MASS) and NRAO VLA Sky Survey (NVSS) up to  $\ell = 5$ . Regions of missing data are accounted for using the sparse inpainting technique described in Starck, Fadili & Rassat 2013, which does not assume the underlying field is either Gaussian or isotropic, but allows for it to be. We focus on the Axis of Evil (AoE) statistic and even/odd mirror parity, both of which search for preferred axes in the Universe. We find that removal of the ISW reduces the significance of these anomalies in WMAP data. There are other signatures of statistical anomalies on large scales that we have not tested (e.g.: north/south asymmetry, cold spot, ...), and exotic physics remain possible. These results are based on WMAP only, and should be repeated with Planck. In the spirit of reproducible research all reconstructed maps and codes will be made available for download here <http://www.cosmostat.org/anomaliesCMB.html>.

## 1. Introduction

In recent years, several violations of statistical isotropy have been reported on the largest scales of the Cosmic Microwave Background (CMB). A low quadrupole was reported in COBE data (Hinshaw et al. 1996; Bond et al. 1998) later confirmed with WMAP data (Spergel et al. 2003). The octopole presented an unusual planarity and its phase seemed correlated with that of the quadrupole (Tegmark et al. 2003; de Oliveira-Costa et al. 2004; Slosar & Seljak 2004; Copi et al. 2010). Other anomalies include a north/south power asymmetry (Eriksen et al. 2004; Bernui et al. 2006), and anomalous cold spot (Vielva et al. 2004; Cruz et al. 2005; Cruz et al. 2006), alignments of other large scale multipoles (Schwarz et al. 2004; Copi et al. 2006), the so-called 'Axis of Evil' (AoE) (Land & Magueijo 2005a) and other violations of statistical isotropy (Hajian & Souradeep 2003; Land & Magueijo 2005b). The very recent Planck results<sup>1</sup> also suggest several of these anomalies are still detected.

These anomalies are interesting because they point towards a possible violation of the standard model of cosmology, which predicts statistical isotropy and Gaussian fluctuations in the CMB, and therefore offer a window into exotic early-universe physics. However, there is still much debate over the possible causes of these anomalies. As these effects

are on very large scales where there is large cosmic variance, the statistics used to measure the significance of the anomalies are subtle (Bennett et al. 2011; Efstathiou et al. 2010; Gold et al. 2011; Hinshaw et al. 2012). They could also be due to some foreground effects, which could either be contamination due to Galactic foregrounds or instrumental effects (Hinshaw et al. 2012; Kim et al. 2012), or cosmological foregrounds which lead to secondary anisotropies in the CMB (Rassat et al. 2007; Rudnick et al. 2007; Peiris & Smith 2010; Smith & Huterer 2010; Yershov et al. 2012; Francis & Peacock 2009; Rassat et al. 2013).

Rassat et al. (2013) investigated simultaneously the impacts of Galactic foregrounds and the integrated Sachs-Wolfe (ISW) effect. Sparse inpainting techniques were used to reconstruct full-sky maps of the CMB and ISW fields. Sparse inpainting does not assume the underlying statistics are Gaussian or isotropic, yet allows for this as a solution (see for e.g., Starck et al. 2013a). Sparse inpainting was shown not to produce spurious ISW effects and provide a bias-free reconstruction method in the context of the tested anomalies (low quadrupole, quadrupole/octopole alignment and octopole planarity). Rassat et al. (2013) found that removal of the ISW reduces the significance of these anomalies in WMAP data, though other hypotheses remain possible (e.g. exotic physics).

In this work we focus on two other claimed anomalies, both related to the preferred axes on the sky: the AoE effect as well as mirror parity. In Section 2 we describe the data

\* anais.rassat@epfl.ch

<sup>1</sup> [http://www.sciops.esa.int/index.php?project=PLANCK&page=Planck\\_Published\\_Papers](http://www.sciops.esa.int/index.php?project=PLANCK&page=Planck_Published_Papers)

used to reconstruct the ISW field from 2MASS and NVSS data. In Section 3, we search for violations of statistical isotropy before and after inpainting, as well as after both inpainting and ISW subtraction. In Section 4 we discuss our results and summarise our results combined with those from Rassat et al. (2013) in Table 1.

## 2. Estimating the Large Scale Primordial CMB

### 2.1. Theory

Since statistical isotropy is predicted for the early Universe, analyses should focus on the primordial CMB, i.e. one from which secondary low-redshift cosmological signals have been removed. In Appendix D, we briefly review how to estimate of the primordial CMB with a reconstructed map of the integrated Sachs-Wolfe effect. In practice, we estimate the primordial CMB on large scales as:

$$\hat{\delta}_{\text{prim}} \simeq \delta_{\text{OBS}} - \hat{\delta}_{\text{ISW}}^{2\text{MASS}} - \hat{\delta}_{\text{ISW}}^{\text{NVSS}} - \delta_{kD, \ell=2}, \quad (1)$$

where  $\hat{\delta}_{\text{ISW}}^{2\text{MASS}}$  and  $\hat{\delta}_{\text{ISW}}^{\text{NVSS}}$  are the estimated ISW contributions from the 2MASS and NVSS surveys (see Section 2.2, Appendix D and Section 2.2 from Rassat et al. 2013, for details on how these are estimated). The terms  $\delta_{\text{OBS}}$  and  $\delta_{\text{prim}}$  correspond to the observed and primordial CMB respectively. The term  $\delta_{kD, \ell=2}$  is the temperature signal due to the kinetic Doppler quadrupole (Copi et al. 2006; Francis & Peacock 2009) and for which we have produced publicly available maps in Rassat et al. (2013).

### 2.2. Data

We are interested in identifying trends and so consider a suite of WMAP renditions from different years, both before and after inpainting. These are the same maps as used in Rassat et al. (2013), described in Appendix A and summarised in Table A.1. The 2MASS (Jarrett 2004) and NVSS (Condon et al. 1998a) data sets used are described in Sections 3.2 and 3.3 or Rassat et al. (2013).

We use the reconstructed ISW effect due to 2MASS and NVSS galaxies, using the method in Dupé et al. (2011) and Rassat et al. (2013), but reconstructing the ISW fields up to  $\ell = 5$ . The ISW reconstruction method is cosmology independent, and estimates the ISW amplitude directly from the CMB and galaxy field cross-correlations. This means that there is a different ISW map for each CMB map rendition considered. All map reconstructions are done using the publicly available ISAP code; the specific options used are described in detail in Rassat et al. (2013).

The large-scale ISW temperature field ( $\ell = 2, 5$ ) due to 2MASS and NVSS data (where the amplitude is estimated with a direct correlation with WMAP9 data) is plotted in Figure 1. Since there is little redshift overlap between the two surveys (see e.g. Figure 3 in Rassat et al. 2013), we estimate the ISW contribution from 2MASS and NVSS independently and then add the two resulting ISW maps to produce the map in Figure 1.

In Figure 2, we plot the amplitude of the ISW temperature power  $C_{\text{TT}}^{\text{ISW}}(\ell)$  for  $\ell = 2, 5$ , which is measured directly from the map plotted in Figure 1. The solid line is the theoretical prediction for a ‘Vanilla-model’ cosmology, taking into account contributions from both 2MASS and NVSS galaxies. Data points are shown for WMAP9, 2MASS and

NVSS data with Gaussian errors bars estimated analytically and assuming  $f_{\text{sky}}^{\text{NVSS}} = 0.66$  (i.e. the smallest  $f_{\text{sky}}$  value amongst the three maps). In general, we find that the ISW signal is below that expected from theory for the fiducial cosmology we have assumed.

## 3. Preferred Axes in WMAP data before and after inpainting and ISW subtraction

We focus on both the Axis of Evil statistic and the even/odd mirror parity anomalies, which are described in detail in Appendix B. In Appendix C, we validate that sparse inpainting provides a bias-free reconstruction with which to study these anomalies using a large set of simulated CMB maps.

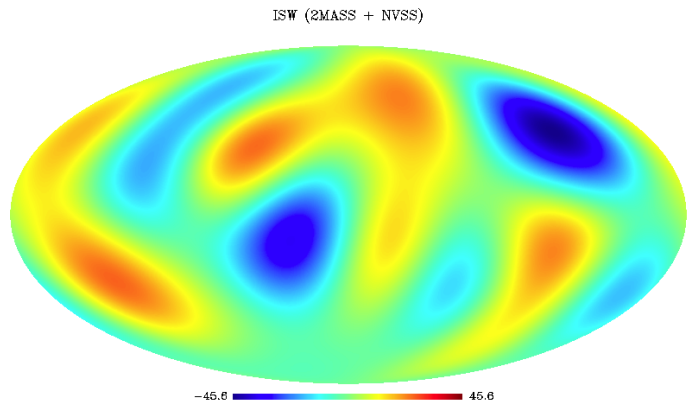


**Fig. 1.** The large-scale ISW temperature field ( $\ell = 2, 5$ ) due to 2MASS and NVSS galaxies. The amplitude is estimated directly from the data, including cross-correlation with WMAP9 data.

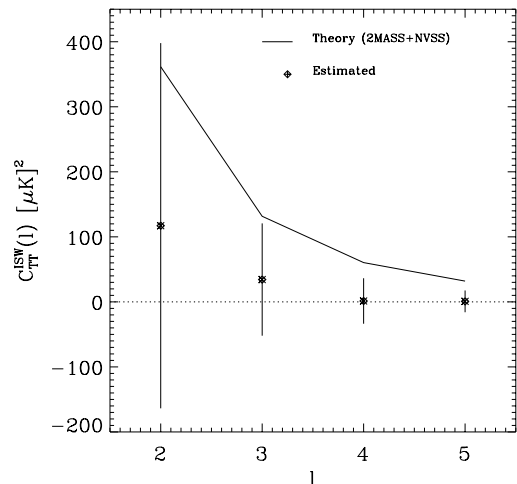


**Fig. 2.** Amplitude of the ISW temperature power  $C_{\text{TT}}^{\text{ISW}}(\ell)$  (in  $\mu K^2$ ) for  $\ell = 2, 5$ . The solid line is the theoretical prediction and the data points are estimated from 2MASS and NVSS galaxies with WMAP9 data are shown with Gaussian error bars assuming  $f_{\text{sky}} = 0.66$ , i.e. the sky coverage of the NVSS survey.

### 3.1. Axis of Evil

Rassat et al. (2007) had searched for an Axis of Evil directly in 2MASS data, hoping that this could link the measured

anomaly to the ISW effect, but had found no preferred axes in 2MASS data. Here, we can test an estimate of the primordial CMB estimated directly.

In Table D.2 we report the preferred modes and axes for the 11 CMB maps considered in this paper. This table can be directly compared with Table 1 in Land & Magueijo (2007) which reviewed the preferred modes and axes for W1 and W3 data. By analysing the ‘raw’ maps (section 1 of Table D.2), we confirm their result that the preferred axis that was present in first year data, is not present in the ILC W3 data. We find the mean interangle is anomalously low for 4 WMAP renditions (TOH1, W5, W7, W9) with  $\theta \sim 20^\circ$ , but that for W3 data,  $\theta \sim 52^\circ$ , similarly to what Land & Magueijo (2007) had found for W1 and W3 maps in their updated analysis of the Axis of Evil. As they had found, the change is due to the fact that the preferred mode for  $\ell = 2$  is  $m = 2$  for W1 (and also years 5 to 9), whereas for W3 data, the preferred mode for  $\ell = 2$  is  $m = 0$ . They attribute this fact to the discontinuous nature of the Axis of Evil statistic, and underline how this feature constitutes a weakness of the Axis of Evil statistic.

However, following Francis & Peacock (2009), we subtract the kinetic Doppler (kD) from the public WMAP maps (i.e. by subtracting the last term in Equation 1) and re-perform the AoE analysis (section 2 of Table D.2, where only the quadrupole  $\ell = 2$  has changed). We find the statistic is now stable across all WMAP data considered, with the mean interangle spanning  $\theta = 18.5 - 20.8^\circ$ .

The results after inpainting of the CMB maps (and kD subtraction) are presented in section 3 of Table D.2. We find inpainting has no effect on the preferred modes and directions for  $\ell = 2$  and  $\ell = 5$ , which are generally unchanged and are the same for all maps, as was the case before inpainting. For  $\ell = 4$ , the preferred mode and direction for all WMAP renditions now becomes similar to that for the TOH map before inpainting. The octopole ( $\ell = 3$ ) is the scale that changes the most after inpainting, both preferred mode and direction are changed for all WMAP renditions. The preferred modes and directions for  $\ell = 2, 5$  are quite stable across all WMAP renditions after inpainting. We note that when searching for quadrupole/octopole alignment, Rassat et al. (2013) showed that the preferred direction of the octopole was stable after inpainting. However, the statistic used there enforces a search within a planar mode ( $m = 3$ ), i.e. using Equation B.1, which explains the difference in stability for the octopole.

The change of only one preferred mode, notably the octopole in the W9 rendition which prefers the planar mode  $m = 3$  rather than  $m = 1$  for other WMAP renditions, has a significant effect on the mean interangle  $\theta$  which changes from  $48.3 - 51.0^\circ$  for W1-7 data to  $16.3^\circ$ , a value which is only found in 0.1% of simulations. Further studies with improved (and smaller) masks, either on WMAP or Planck data could point as to why the AoE statistic on W9 data is so different.

The results after inpainting and ISW subtraction are presented in section 4 of Table D.2. For the quadrupole, the preferred mode remains the same, and the preferred direction changes slightly. For  $\ell = 4, 5$  there is virtually no change in either the preferred mode or direction, which can be explained by the low values of the ISW signal on these scales (see Figure 2). The scale with most change is the octopole, where both preferred mode and direction change for all WMAP renditions. In general, there is good

agreement across different WMAP renditions, except some differences for the octopole, e.g. for W3 and W9 renditions. After inpainting and ISW subtraction the mean interangle now varies between  $33.1 - 47.8$ , which corresponds to  $1.9 - 13.3\%$  of values found in simulations. Even for the lowest value of 1.9%, the original anomalous alignment is no longer as significant as the previous value of 0.1% on the ILC maps.

### 3.2. Parity

We calculate the  $S_{\pm}$  values for each of the WMAP renditions using Equations B.4, B.5 and B.6, and results are presented in Table D.1, where the significance is calculated using 1000 full-sky Gaussian realisations. Before inpainting (part 1 of Table D.1), we find no significant even ( $S_{+}$ ) or odd ( $S_{-}$ ) mirror parity, except for the TOH map which shows a mild preference for even mirror parity (only 2.6% of simulations have a higher  $S_{+}$  value). After sparse inpainting (part 2 of Table D.1), we find an increase in both even and odd mirror parity anomalies (except for the TOH map), with only 3.2 – 3.6% of simulations having a higher value for  $S_{-}$  than both W7 and W9 maps and only 0.90 – 3.1% of simulations having a higher value for  $S_{+}$ . The significance of these remains at  $< 3\sigma$  though. We find the mirror-parity anomalies do not persist after sparse inpainting and subtraction of the reconstructed ISW signal (part 3 of Table D.1), meaning the ISW could explain these anomalies.

## 4. Discussion

One of the main successes of the standard model of cosmology, is its prediction of the Gaussian random fluctuations observed in the CMB. However, even since COBE data, several signatures of lack of statistic isotropy, or ‘anomalies’ have been reported on large scales in WMAP data, though their significance is widely debated. Recent focus has been on testing the impact of different reconstruction methods or methods for dealing with Galactic foregrounds, while other have investigated how various foreground cosmological signals could impact these anomalies.

In Rassat et al. (2013), we proposed an update to the work of Francis & Peacock (2009) and Kim et al. (2012), by considering the following issues:

1. Tomography: ISW reconstruction due to both 2MASS (Jarrett 2004) and NVSS (Condon et al. 1998a) data.
2. Trends: Identifying trends amongst 11 WMAP renditions, including 6 using the sparse inpainting technique mentioned below
3. Sparse Inpainting: Missing data in CMB and LSS maps were reconstructed using sparse inpainting, which does not assume the data is Gaussian or statistically isotropic
4. Tests for biases: for the statistical anomalies considered, sparse inpainting was shown to provide a bias-free reconstruction.

Rassat et al. (2013) investigated three previously claimed anomalies: the low quadrupole, the quadrupole/octopole alignment and the octopole planarity, and showed that removal of the ISW reduces the significance of these anomalies in WMAP data, though other hypotheses such as exotic physics remain possible too.

In this work, we continue the investigation of two other previously claimed anomalies, both related to preferred

axes in the sky: the Axis of Evil (AoE) and even/odd mirror parity in CMB data, i.e. parity with respect to reflections through a plane.

We first investigate whether sparse inpainting can be considered a bias-free reconstruction method for the two statistics and find that this is the case. We then apply sparse inpainting on various CMB maps up to  $\ell = 5$  and reconstruct the ISW maps from 2MASS and NVSS data also up to  $\ell = 5$ . We consider the significance of both reported anomalies, before inpainting, after inpainting and both after inpainting and ISW subtraction.

Our first approach to the AoE is to remove the kD quadrupole (following Francis & Peacock 2009), and we find that the AoE is consistent across all renditions WMAP data (TOH, W3, W5, W7 and W9), contrarily to what Land & Magueijo (2007) had found. After sparse inpainting, we find the AoE is no longer anomalous, mainly due to the change in preferred mode and axis of the octopole, except for WMAP9 data, where the anomaly persists. Further studies with improved (and smaller) masks, either on WMAP or Planck data, could point as to why the AoE statistic on WMAP9 data is so different. After sparse inpainting, both even and odd mirror parities are increased in significance, but not enough to be considered significantly anomalous.

We find that subtraction of the ISW effect due to 2MASS and NVSS galaxies, reduced the significance of these anomalies. These results, along with those in Rassat et al. (2013) relating to the low quadrupole, the quadrupole/octopole alignment and the octopole planarity are summarised in Table 1. We note however, that there are other signatures of statistical anomalies on large scales that we have not tested (e.g.: north/south asymmetry, cold spot, ...) and that exotic physics remain possible. These results are based on WMAP only, and should be repeated with Planck.

In the spirit of reproducible research all reconstructed maps and codes which constitute the main results of this paper will be made available for download here <http://www.cosmostat.org/anomaliesCMB.html>.

Anomaly	After Sparse Inpainting	After ISW Subtraction
<i>From Rassat et al. (2013)</i>		
Press Low Quad	More Anomalous	Not Anomalous
Quad/Oct Alignment	Less Anomalous	Not Anomalous
Oct planarity	Less Anomalous	Not Anomalous
<i>This work</i>		
Axis of Evil	Less Anomalous	Not Anomalous
Even Mirror Parity	More Anomalous	Not Anomalous
Odd Mirror Parity	More Anomalous	Not Anomalous

**Table 1.** Summary of results in this paper and Rassat et al. (2013). The anomalies in WMAP could be explained by the ISW effect, though other explanations remain possible.

*Acknowledgements.* We use iCosmo<sup>2</sup>, Healpix (Górski et al. 2002; Gorski et al. 2005), ISAP<sup>3</sup>, 2MASS<sup>4</sup>, WMAP<sup>5</sup> and NVSS data<sup>6</sup> and the Galaxy extinction maps of Schlegel et al. (1998). This research is in part supported by the European Research Council grant SparseAstro (ERC-228261) and by the Swiss National Science Foundation (SNSF).

<sup>2</sup> <http://www.icosmo.org>, Refregier et al. (2011)

<sup>3</sup> <http://jstarck.free.fr/isap.html>

<sup>4</sup> <http://www.ipac.caltech.edu/2mass/>

<sup>5</sup> <http://map.gsfc.nasa.gov>

<sup>6</sup> <http://heasarc.gsfc.nasa.gov/W3Browse/all/nvss.html>

## References

- Abrial, P., Moudden, Y., Starck, J.-L., et al. 2008, *Statistical Methodology*, 5, 289
- Ben-David, A., Kovetz, E. D., & Itzhaki, N. 2012, *ApJ*, 748, 39
- Bennett, C. L., Hill, R. S., Hinshaw, G., et al. 2011, *ApJS*, 192, 17
- Bernui, A., Vilella, T., Wuensche, C. A., Leonardi, R., & Ferreira, I. 2006, *A&A*, 454, 409
- Bond, J. R., Jaffe, A. H., & Knox, L. 1998, *Phys. Rev. D*, 57, 2117
- Boughn, S. P., Crittenden, R. G., & Turok, N. G. 1998, *New A*, 3, 275
- Bucher, M. & Louis, T. 2012, *MNRAS*, 424, 1694
- Cabr e, A., Fosalba, P., Gazta naga, E., & Manera, M. 2007, *MNRAS*, 381, 1347
- Condon, J. J., Cotton, W. D., Greisen, E. W., et al. 1998a, *AJ*, 115, 1693
- Condon, J. J., Cotton, W. D., Greisen, E. W., et al. 1998b, *AJ*, 115, 1693
- Copi, C. J., Huterer, D., Schwarz, D. J., & Starkman, G. D. 2006, *Mon. Not. Roy. Astron. Soc.*, 367, 79
- Copi, C. J., Huterer, D., Schwarz, D. J., & Starkman, G. D. 2010, *Advances in Astronomy*, 2010
- Cruz, M., Mart nez-Gonz lez, E., Vielva, P., & Cay n, L. 2005, *MNRAS*, 356, 29
- Cruz, M., Tucci, M., Mart nez-Gonz lez, E., & Vielva, P. 2006
- de Oliveira-Costa, A., Tegmark, M., Zaldarriaga, M., & Hamilton, A. 2004, *Phys. Rev. D*, 69, 063516
- Delabrouille, J., Cardoso, J., Le Jeune, M., et al. 2009, *A&A*, 493, 835
- Dup e, F.-X., Rassat, A., Starck, J.-L., & Fadili, M. J. 2011, *A&A*, 534, A51
- Efstathiou, G., Ma, Y.-Z., & Hanson, D. 2010, *MNRAS*, 407, 2530
- Eriksen, H. K., Hansen, F. K., Banday, A. J., Gorski, K. M., & Lilje, P. B. 2004, *Astrophys. J.*, 605, 14
- Francis, C. L. & Peacock, J. A. 2009, *ArXiv e-prints*
- Giannantonio, T., Scranton, R., Crittenden, R. G., et al. 2008, *PRD*, 77, 123520
- Gold, B., Bennett, C. L., Hill, R. S., et al. 2009, *ApJS*, 180, 265
- Gold, B., Odegard, N., Weiland, J. L., et al. 2011, *ApJS*, 192, 15
- G rski, K. M., Banday, A. J., Hivon, E., & Wandelt, B. D. 2002, in *Astronomical Society of the Pacific Conference Series*, Vol. 281, *Astronomical Data Analysis Software and Systems XI*, ed. D. A. Bohlender, D. Durand, & T. H. Handley, 107–+
- Gorski, K. M. et al. 2005, *Astrophys. J.*, 622, 759
- Hajian, A. & Souradeep, T. 2003, *ApJ*, 597, L5
- Hinshaw, G., Branday, A. J., Bennett, C. L., et al. 1996, *ApJ*, 464, L25+
- Hinshaw, G., Larson, D., Komatsu, E., et al. 2012, *ArXiv e-prints*
- Hinshaw, G., Nolta, M. R., Bennett, C. L., et al. 2007, *ApJS*, 170, 288
- Jarrett, T. 2004, *Publications of the Astronomical Society of Australia*, 21, 396
- Kim, J., Naselsky, P., & Mandolesi, N. 2012, *ApJ*, 750, L9
- Land, K. & Magueijo, J. 2005a, *Phys. Rev. Lett.*, 95, 071301
- Land, K. & Magueijo, J. 2005b, *Mon. Not. Roy. Astron. Soc.*, 357, 994
- Land, K. & Magueijo, J. 2005, *Phys. Rev. Lett.*, 72, 101302
- Land, K. & Magueijo, J. 2007, *MNRAS*, 378, 153
- Peiris, H. V. & Smith, T. L. 2010, *Phys. Rev. D*, 81, 123517
- Plaszczynski, S., Lavabre, A., Perotto, L., & Starck, J.-L. 2012, *A&A*, 544, A27
- Rassat, A., Land, K., Lahav, O., & Abdalla, F. B. 2007, *MNRAS*, 377, 1085
- Rassat, A., Starck, J.-L., & Dupe, F.-X. 2013, *ArXiv e-prints*
- Refregier, A., Amara, A., Kitching, T. D., & Rassat, A. 2011, *A&A*, 528, A33+
- Rossmannith, G., Modest, H., R ath, C., et al. 2012, *Phys. Rev. D*, 86, 083005
- Rudnick, L., Brown, S., & Williams, L. R. 2007, *ApJ*, 671, 40
- Schlegel, D. J., Finkbeiner, D. P., & Davis, M. 1998, *Astrophys. J.*, 500, 525
- Schwarz, D. J., Starkman, G. D., Huterer, D., & Copi, C. J. 2004, *Physical Review Letters*, 93, 221301
- Slosar, A. & Seljak, U. 2004, *Phys. Rev. D*, 70, 083002
- Smith, K. M. & Huterer, D. 2010, *MNRAS*, 403, 2
- Spergel, D. N. et al. 2003, *Astrophys. J. Suppl.*, 148, 175
- Starck, J.-L., Donoho, D. L., Fadili, M. J., & Rassat, A. 2013a, *ArXiv e-prints*
- Starck, J.-L., Fadili, M. J., & Rassat, A. 2013b, *A&A*, 550, A15

Starck, J.-L., Murtagh, F., & Fadili, M. 2010, Sparse Image and Signal Processing (Cambridge University Press)

Tegmark, M., de Oliveira-Costa, A., & Hamilton, A. 2003, Phys. Rev., D68, 123523

Vielva, P., Martínez-González, E., Barreiro, R. B., Sanz, J. L., & Cayón, L. 2004, ApJ, 609, 22

Yershov, V. N., Orlov, V. V., & Raikov, A. A. 2012, MNRAS, 3083

Zacchei, A., Maino, D., Baccigalupi, C., et al. 2011, A&A, 536, A5

## Appendix A: WMAP Cosmic Microwave Background Maps Considered

As we are interested in identifying trends in the data, we consider a suite of 11 different renditions of WMAP data. These are summarised in Table A.1 and are: the Tegmark et al. (2003) reduced-foreground CMB Map (TOH1), the Internal Linear Combination (ILC) WMAP maps from the 3rd year (ILC W3, Hinshaw et al. 2007), 5th year (ILC W5, Gold et al. 2009), 7th year (ILC W7, Gold et al. 2011), and the 9th year (ILC W9, Hinshaw et al. 2012), as well as sparsely inpainted versions of these maps. We also consider the sparsely inpainted WMAP ILC 5th year data reconstructed by (Dela W5, Delabrouille et al. 2009) using wavelets.

## Appendix B: Statistical Anomalies & Impact of Sparse inpainting

### B.1. Preferred Axis for Low Multipoles: Axis of Evil

It was first noted by de Oliveira-Costa et al. (2004) that both the quadrupole and octopole of the CMB appeared planar (i.e. anomalously dominated by  $m = \pm\ell$  modes) and were also aligned along a similar axis. This can be measured by maximising the statistic (de Oliveira-Costa et al. 2004):

$$q_\ell(\hat{\mathbf{n}}) = \sum_m m^2 |a_{\ell m}(\hat{\mathbf{n}})|^2, \quad (\text{B.1})$$

where  $a_{\ell m}(\hat{\mathbf{n}})$  corresponds to the  $a_{\ell m}$  coefficients of the rotated CMB temperature anisotropy map where  $\hat{\mathbf{n}}$  corresponds to the new z-axis of the rotated map. By maximising  $q_\ell(\hat{\mathbf{n}})$  one finds the preferred axis  $\hat{\mathbf{n}}$ . The term  $m^2$  ensures that planar modes are favoured in the search of the preferred axis. Land & Magueijo (2005a) suggested an alternative statistic, where the preferred axis can be found by considering an anomalous concentration of power in *any* mode  $m$ , instead of focussing on planar modes. This can be quantified by considering their statistic:

$$r_\ell = \max_{m, \hat{\mathbf{n}}} \frac{C_{\ell m}(\hat{\mathbf{n}})}{(2\ell + 1)\hat{C}_\ell}. \quad (\text{B.2})$$

The expressions  $C_{\ell m}(\hat{\mathbf{n}})$  are given by  $C_{\ell 0}(\hat{\mathbf{n}}) = |a_{\ell 0}(\hat{\mathbf{n}})|^2$  and  $C_{\ell m}(\hat{\mathbf{n}}) = 2|a_{\ell m}(\hat{\mathbf{n}})|^2$  for  $m > 0$  and  $(2\ell + 1)\hat{C}_\ell = \sum_m |a_{\ell m}|^2$ . The above statistic finds both a preferred axis  $\hat{\mathbf{n}}$ , as well as a preferred mode  $m$ , whereas Equation B.1 favours the  $m = \ell$  mode. As discussed in Land & Magueijo (2005a), the statistic is never ambiguous except for planar quadrupoles which can be interpreted as  $m = 2$  or  $m = 1$  modes with the preferred axis  $\hat{\mathbf{n}}_2$  rotated by  $90^\circ$ . Following their convention, we adopt the  $m = 2$  configuration for quadrupoles where the  $m = 1$  or  $m = 2$  mode is favoured. This choice also ensures one can reproduce the

quadrupole/octopole planarity previously reported by de Oliveira-Costa et al. (2004).

Land & Magueijo (2005a) found the preferred axes for  $\ell = 2, \dots, 5$  for WMAP 1 data seemed aligned along a similar axis in the direction of  $(\ell, b) \sim (-100^\circ, 60^\circ)$ , where the  $l$  varied from  $\simeq [-90^\circ, -160^\circ]$  and  $b$  varied from  $\simeq [48^\circ, 62^\circ]$ . By considering the mean interangle  $\theta$  (i.e. the mean value of all possible angles between two axes  $\hat{\mathbf{n}}_\ell$  and  $\hat{\mathbf{n}}_{\ell'}$  for  $\ell, \ell' = 2, \dots, 5$  and  $\ell \neq \ell'$ ), they found that only 0.1% of simulations had an average value smaller than the one measured in WMAP1 data ( $\sim 20^\circ$ ) and therefore rejected statistical isotropy at the 99.9% confidence level. The preferred axis has been dubbed the ‘‘Axis of Evil’’.

### B.2. Mirror Parity

Another property to consider is mirror parity in CMB data, i.e. parity with respect to reflections through a plane:  $\hat{\mathbf{x}} = \hat{\mathbf{x}} - 2(\hat{\mathbf{x}} \cdot \hat{\mathbf{n}})\hat{\mathbf{n}}$ , where  $\hat{\mathbf{n}}$  is the normal vector to the plane.

Since mirror parity is yet another statistic for which preferred axes can be found (i.e. the normal to the plane of reflection), it is complementary to the search for a preferred axis described in Section B.1. For example, it is interesting to assess whether existing preferred axes are also endowed with mirror parity handedness, or search for any other mirror parity preferred axes. In practice, mirror parity and preferred axes found using Equation B.2 are statistically independent (Land & Magueijo 2005), and so coincidental presence of both will increase the significance of the Axis of Evil / mirror parity anomaly.

With all-sky data, one can estimate the  $S$ -map for a given multipole by:

$$\tilde{S}_\ell(\hat{\mathbf{n}}) = \sum_{m=-\ell}^{\ell} (-1)^{\ell+m} \frac{|a_{\ell m}(\hat{\mathbf{n}})|^2}{\hat{C}_\ell}, \quad (\text{B.3})$$

where  $a_{\ell m}(\hat{\mathbf{n}})$  corresponds to the value of the  $a_{\ell m}$  coefficients when the map is rotated to have  $\hat{\mathbf{n}}$  as the z-axis. Positive (negative) values of  $\tilde{S}_\ell(\hat{\mathbf{n}})$  correspond to even (odd) mirror parities in the  $\hat{\mathbf{n}}$  direction. The same statistic can also be considered summed over all low multipoles one wishes to consider (e.g. the multipoles which have similar preferred axes) as in Ben-David et al. (2012):

$$\tilde{S}_{\text{tot}}(\hat{\mathbf{n}}) = \sum_{\ell=2}^{\ell_{\text{max}}} \tilde{S}_\ell(\hat{\mathbf{n}}). \quad (\text{B.4})$$

It is convenient to redefine the parity estimator as  $S(\hat{\mathbf{n}}) = \tilde{S}_{\text{tot}}(\hat{\mathbf{n}}) - (\ell_{\text{max}} - 1)$ , so that  $\langle S \rangle = 0$ .

The most even and odd mirror-parity directions for a given map can be considered by estimating (Ben-David et al. 2012):

$$S_+ = \frac{\max(S) - \mu(S)}{\sigma(S)}, \quad (\text{B.5})$$

$$S_- = \frac{|\min(S) - \mu(S)|}{\sigma(S)}, \quad (\text{B.6})$$

where  $\mu(S)$  and  $\sigma(S)$  are the mean and standard deviation of the  $S$  map. The quantities  $S_+$  and  $S_-$  each correspond to different axes  $\hat{\mathbf{n}}_+$  and  $\hat{\mathbf{n}}_-$  respectively.

Others have also studied point-parity with different statistics, e.g. Land & Magueijo (2005) who did not find

Label	WMAP Year	Mask Treatment	Reference
TOH W1	W1	ILC	Tegmark et al. (2003)
ILC W3	W3	ILC	Hinshaw et al. (2007)
ILC W5	W5	ILC	Gold et al. (2009)
ILC W7	W7	ILC	Gold et al. (2011)
Te ILC W9	W9	ILC	Hinshaw et al. (2012)
TOH W1 (inp)	W1	ILC + Sparse inpainting	This work
ILC W3 (inp)	W3	ILC + Sparse inpainting	This work
ILC W5 (inp)	W5	ILC + Sparse inpainting	This work
Dela W5 (inp)	W5	ILC-Wavelets + Sparse inpainting	This work
ILC W7 (inp)	W7	ILC + Sparse inpainting	This work
ILC W9 (inp)	W9	ILC + Sparse inpainting	This work

**Table A.1.** : List of the 11 temperature anisotropy maps we use to probe the anomalies in the primordial CMB, including year of WMAP data they correspond to and a description of the mask treatment. ‘TOH’ corresponds to the treatment in Tegmark et al. (2003), ‘ILC’ to the Internal Linear Combination method (see Hinshaw et al. 2007, 2012; Gold et al. 2009, 2011), ‘ILC-Wavelets’ corresponds to the method in Delabrouille et al. (2009) and the sparse inpainting method is described in A08-SMF10 and uses the sparsity prior described in Starck, Fadili, & Rassat (2013b).

significant point-parity in the first WMAP data release. ??? however, found evidence for odd point parity in later WMAP renditions, and linked this anomaly with the low level of correlations on the largest scales.

### Appendix C: Validation of Sparse Inpainting to Study Large Scale Anomalies

One can test for preferred axes directly on different renditions of WMAP data, for example on Internal Linear Combination (ILC) maps. However, these may be contaminated on large scales due to Galactic foregrounds (Hinshaw et al. 2012). Another approach is to use a different basis set than spherical harmonics, i.e. use a basis that is orthonormal on a cut sky (e.g. Rossmanith et al. 2012). Alternatively, one can use sparse inpainting techniques to reconstruct full-sky maps (Plaszczynski et al. 2012; Dupé et al. 2011; Rassat et al. 2013) or other inpainting methods such as diffuse inpainting (Zacchei et al. 2011) or inpainting using constrained Gaussian realisations (Bucher & Louis 2012; Kim et al. 2012). Any inpainting technique should be tested for potential biases, specifically for the masks and statistical tests one is interested in. Here we use the sparse inpainting techniques first described in Abrial et al. (2008) and Starck, Murtagh, & Fadili (2010) and refined in Starck, Fadili, & Rassat (2013b) to reconstruct regions of missing data. The advantage of this method is that it does not assume the ‘true’ map is either Gaussian or isotropic, yet it allows it to be (see for e.g. Starck et al. 2013a).

Rassat et al. (2013) showed that sparse inpainting was a bias-free reconstruction method for the low quadrupole, quadrupole/octopole alignment and octopole planarity tests. Here, we test whether sparse inpainting is a bias-free reconstruction method for both the Axis of Evil statistic and mirror parity. We calculate 1000 Gaussian Random Field realisations of WMAP7 best fit cosmology using the WMAP7 temperature analysis mask ( $f_{\text{sky}} = 0.78$ ).

#### C.1. Recovering the Mean Interangle ( $\theta$ ) with a realistic Galactic mask

We compare the mean interangle  $\theta$  for the statistic given in Equation B.2 for  $\ell = 2 - 5$ , for each map before and after inpainting using  $n_{\text{side}} = 128$  for the CMB maps.

The mean interangle for our simulations before and after inpainting is  $\sim 57^\circ \pm 9^\circ$ , i.e. what is expected in the case of isotropic axes and a Gaussian random field (Land & Magueijo 2005a). After inpainting with the WMAP7 mask we find that  $(\theta_{\text{true}} - \theta_{\text{inp}}) \sim -0.55^\circ \pm 10.7^\circ$ , showing there is no significant bias in the estimation of the mean interangle after sparse inpainting is applied. While the bias is small, the error bar on the mean interangle after sparse inpainting is not negligible ( $10^\circ$ ). Following Starck, Fadili, & Rassat (2013b), we also test the statistic on an optimistic Planck-like mask with  $f_{\text{sky}} = 0.93$  and find  $(\theta_{\text{true}} - \theta_{\text{inp}}) \sim 0.17^\circ \pm 7.3^\circ$ , showing we can expect better reconstructions with future Planck data and smaller masks.

#### C.2. Recovering Mirror Parity Statistics ( $S_{\pm}$ ) with a realistic Galactic mask

In order to test for possible biases in the  $S_{\pm}$  statistics after sparse inpainting, we calculate  $S_+$  and  $S_-$  for each CMB simulation before and after inpainting, setting  $n_{\text{side}} = 8$  for the CMB maps, and  $n_{\text{side}} = 64$  for the parity maps (calculated using Equation B.3), as in Ben-David et al. (2012). As in Figure 6 of Ben-David et al. (2012), we find that the distributions of  $S_+$  and  $S_-$  populations do not change before and after inpainting (‘True’ and ‘After Inp.’ columns in Table C.1). We also do not find any significant bias in the  $S_{\pm}$  measurements (‘Bias’ column in Table C.1).

	True	After Inp.	Bias
$\theta$	$57.5^\circ \pm 9.2^\circ$	$57.0^\circ \pm 9.2^\circ$	$0.55^\circ \pm 10.7^\circ$
$S_+$	$2.59 \pm 0.30$	$2.59 \pm 0.30$	$-0.00039 \pm 0.22$
$S_-$	$2.81 \pm 0.35$	$2.82 \pm 0.35$	$-0.0049 \pm 0.26$

**Table C.1.** Mean interangle  $\theta$  for the ‘Axis of Evil’ statistic and even (+) and odd (−) mirror parity statistics  $S_{\pm}$  before and after sparse inpainting on 1000 Gaussian random field realisations of CMB data and using the WMAP7 temperature analysis mask for the inpainted maps. The bias is taken by considering the difference (true − inp).

Following Starck, Fadili, & Rassat (2013b), we also test the statistic on an optimistic Planck-like mask with  $f_{\text{sky}} = 0.93$  and find  $\Delta S_+ = -0.0021 \pm 0.081$  and  $\Delta S_- =$

$0.00091 \pm 0.10$ , showing we can expect significantly better reconstructions with future Planck data and smaller masks.

## Appendix D: Recovering the Primordial CMB

Since statistical isotropy is predicted for the early Universe, analyses should focus on the primordial CMB, i.e. one from which secondary low-redshift cosmological signals has been removed. The observed temperature anisotropies in the CMB,  $\delta_{\text{OBS}}$ , can be described as the sum of several components:

$$\delta_{\text{OBS}} = \delta_{\text{prim}} + \delta_{\text{ISW}}^{\text{total}} + \delta_{\text{other}} + \mathcal{N}, \quad (\text{D.1})$$

where  $\delta_{\text{prim}}$  are the primordial temperature anisotropies,  $\delta_{\text{ISW}}^{\text{total}}$  are the total secondary temperature anisotropies due to the late-time Integrated Sachs Wolfe (ISW) effect,  $\delta_{\text{other}}$  are other secondary anisotropies (e.g. the Sunyaev-Zel'dovich effect) and  $\mathcal{N}$  is the noise. On large scales the ISW signal is the only secondary anisotropy and the anisotropies are cosmic variance limited, so that the last two terms can be ignored:

$$\delta_{\text{OBS}} = \delta_{\text{prim}} + \delta_{\text{ISW}}^{\text{total}} \quad \text{for large scales.} \quad (\text{D.2})$$

The late time ISW effect arises in universes where the cosmic potential  $\Phi$  decays at late times, as is the case in universes with dark energy, open curvature or possibly in some modified gravities. The temperature fluctuations due to the late ISW effect are given by:

$$\delta_{\text{ISW}}^{\text{total}} = -2 \int_{\eta_L}^{\eta_0} \Phi'((\eta_0 - \eta)\hat{\mathbf{n}}) d\eta, \quad (\text{D.3})$$

where  $\eta$  is the conformal time, defined by  $d\eta = \frac{dt}{a(t)}$  and  $\eta_0$  and  $\eta_L$  are the conformal times today and at the surface of last scattering. The unit vector  $\hat{\mathbf{n}}$  is along the line of sight and the gravitational potential  $\Phi(\mathbf{x}, \eta)$  depends on both position and time. The integral depends on the rate of change of the potential  $\Phi' \equiv \frac{d\Phi}{d\eta}$ , which is non-null in universes with dark energy, non-flat curvature and some models of modified gravity. The potential  $\Phi$  can be related to the matter field, of which a galaxy map is assumed to be a tracer.

In practice, the temperature ISW field can be reconstructed in spherical harmonics,  $\delta_{\ell m}^{\text{ISW}}$ , from the LSS field  $g_{\ell m}$  (Boughn et al. 1998; Cabré et al. 2007; Giannantonio et al. 2008):

$$\delta_{\ell m}^{\text{ISW}} = \frac{C_{gT}(\ell)}{C_{gg}(\ell)} g_{\ell m}, \quad (\text{D.4})$$

where  $g_{\ell m}$  represent the spherical harmonic coefficients of a galaxy overdensity field  $g(\theta, \phi)$ , given by

$$g(\theta, \phi) = \sum_{\ell, m} g_{\ell m} Y_{\ell m}(\theta, \phi), \quad (\text{D.5})$$

where  $Y_{\ell m}(\theta, \phi)$  are the spherical harmonics. The spectra  $C_{gg}$  and  $C_{gT}$  are the galaxy (g) and CMB (T) auto- and cross-correlations measured from the data or their theoretical values given by:

$$C_{gT}(\ell) = 4\pi b_g \int dk \frac{\Delta^2(k)}{k} W_g(k) W_T(k), \quad (\text{D.6})$$

$$C_{gg}(\ell) = 4\pi b_g^2 \int dk \frac{\Delta^2(k)}{k} [W_g(k)]^2, \quad (\text{D.7})$$

where

$$W_g(k) = \int dr \Theta(r) j_\ell(kr) D(z), \quad (\text{D.8})$$

$$W_T(k) = -\frac{3\Omega_{m,0} H_0^2}{k^2 c^3} \int_0^{z_L} dr j_\ell(kr) H(z) D(z) (f-1), \quad (\text{D.9})$$

$$\Delta^2(k) = \frac{4\pi}{(2\pi)^3} k^3 P(k), \quad (\text{D.10})$$

$$\Theta(r) = \frac{r^2 n(r)}{\int dr r^2 n(r)}, \quad (\text{D.11})$$

where we use the same notation as in Rassat et al. (2007) and have assumed a linear bias  $b(k, z) \equiv b_g$  and  $D(z)$  is the linear growth function.

From Equation D.4, we can check that:

$$\langle \delta_{\ell m}^{\text{ISW}} g_{\ell m}^* \rangle = C_{gT}(\ell), \quad (\text{D.12})$$

and

$$\langle \delta_{\ell m}^{\text{ISW}} \delta_{\ell m}^{*\text{ISW}} \rangle = \frac{C_{gT}^2(\ell)}{C_{gg}(\ell)} = C_{\text{ISW}}(\ell). \quad (\text{D.13})$$

Equation D.4 and D.13 show that the ISW temperature field is independent of the galaxy bias  $b_g$ , which relates the galaxy and matter (m) fluctuations by  $g_{\ell m} = b_g \delta_{m, \ell m}$ , and that it is not necessary to estimate the value of the galaxy bias in order to estimate the ISW temperature field.

Map	$S_+$	$S_-$
1) Before inpainting		
TOH1	3.25 (2.6%)	3.15 (16%)
WMAP3	2.88 (17%)	2.81 (48%)
WMAP5	2.93 (14%)	2.85 (43%)
WMAP7	2.93 (14%)	2.88 (39%)
WMAP9	3.00 (9.9%)	2.93 (34%)
2) After inpainting		
TOH1 (inp)	3.09 (5.7%)	3.29 (10%)
WMAP3 (inp)	3.31 (1.9%)	3.39 (6.5%)
WMAP5 (inp)	3.30 (2.0%)	3.40 (6.1%)
W5 Dela (inp)	3.41 (0.90%)	3.57 (3.1%)
WMAP7 (inp)	3.34 (1.4%)	3.55 (3.2%)
WMAP9 (inp)	3.20 (3.1%)	3.54 (3.6%)
3) After inpainting and ISW subtraction		
TOH1 (inp) - ISW	2.87 (17%)	3.21 (13%)
WMAP3 (inp) - ISW	2.94 (13%)	3.20 (14%)
WMAP5 (inp) - ISW	3.05 (7.5%)	3.26 (11%)
W5 Dela (inp) - ISW	3.01 (9.3%)	3.25 (11%)
WMAP7 (inp) - ISW	3.01 (9.3%)	3.37 (7.3%)
WMAP9 (inp) - ISW	2.92 (14%)	3.40 (6.1%)

**Table D.1.** Values of even ( $S_+$ ) and odd ( $S_-$ ) parity scores for  $2 < \ell < 5$  for WMAP data from different years before (1) and after inpainting (2), and after subtraction of the ISW effect due to both 2MASS and NVSS galaxies (3). The occurrence for 1000 full-sky Gaussian random simulations is given in brackets. For all maps the kD quadrupole has been subtracted.

Map	Mean Interangle $\theta$ ( $^\circ$ )	$\ell = 2$ ( $b, l$ )	$m$	$\ell = 3$ ( $b, l$ )	$m$	$\ell = 4$ ( $b, l$ )	$m$	$\ell = 5$ ( $b, l$ )	$m$
Before Inpainting									
1)									
TOH1	20.9	(58.9, -103.4)	2	(61.9, -104.8)	3	(57.8, -164.0)	2	(47.7, -132.6)	3
W3	51.9	(-27.4, 3.3)	0	(62.3, -103.8)	3	(34.6, -132.2)	1	(47.4, -129.9)	3
W5	19.7	(61.2, -121.7)	2	(62.3, -103.8)	3	(34.2, -131.8)	1	(47.4, -129.9)	3
W7	20.4	(62.7, -123.4)	2	(62.7, -104.0)	3	(33.9, -131.5)	1	(47.4, -130.7)	3
W9	19.1	(60.1, -120.6)	2	(62.7, -105.2)	3	(34.2, -131.1)	1	(47.7, -130.2)	3
2)									
TOH1 - kD	20.8	(56.6, -106.5)	2	-	-	-	-	-	-
W3 - kD	20.3	(62.7, -129.5)	2	-	-	-	-	-	-
W5 - kD	18.9	(57.8, -125.7)	2	-	-	-	-	-	-
W7 - kD	19.5	(58.5, -127.6)	2	-	-	-	-	-	-
W9 - kD	18.5	(57.0, -124.9)	2	-	-	-	-	-	-
After Inpainting									
3)									
TOH1 (inp) - kD	51.0	(48.5, -116.4)	2	(29.3, 82.6)	1	(57.8, -168.1)	2	(47.4, -140.0)	3
W3 (inp) - kD	48.3	(59.7, -140.0)	2	(31.7, 81.6)	1	(58.2, -165.9)	2	(47.0, -135.0)	3
W5 (inp) - kD	49.0	(54.7, -135.0)	2	(31.4, 81.9)	1	(58.2, -165.9)	2	(47.0, -135.0)	3
Dela W5 (inp) - kD	49.0	(54.0, -140.6)	2	(28.0, 82.6)	1	(58.9, -166.6)	2	(46.2, -135.8)	3
W7 (inp) - kD	48.5	(55.5, -138.9)	2	(30.7, 82.6)	1	(58.2, -165.9)	2	(47.0, -135.8)	3
W9 (inp) - kD	16.3	(54.7, -135.0)	2	(57.8, -116.4)	3	(58.2, -165.9)	2	(47.4, -135.4)	3
4)									
TOH1 (inp) - kD - ISW	33.1	(79.0, -175.5)	2	(26.6, -176.8)	2	(57.8, -168.1)	2	(47.4, -137.0)	3
W3 (inp) - kD - ISW	35.2	(75.7, 148.8)	2	(26.3, -177.2)	2	(58.2, -166.9)	2	(47.0, -135.0)	3
W5 (inp) - kD - ISW	47.8	(74.6, 161.8)	2	(20.1, -76.3)	2	(58.2, -166.9)	2	(47.0, -135.0)	3
Dela W5 (inp) - kD - ISW	32.6	(72.0, 162.6)	2	(27.0, -177.9)	2	(58.5, -167.8)	2	(46.2, -135.8)	3
W7 (inp) - kD - ISW	33.4	(74.2, 158.0)	2	(27.0, -177.2)	2	(57.8, -167.1)	2	(47.0, -135.8)	3
W9 (inp) - kD - ISW	44.1	(75.0, 161.3)	2	(54.7, 45.9)	2	(57.8, -167.1)	2	(47.7, -135.8)	3

**Table D.2.** Preferred axes for multipoles  $\ell = 2 - 5$  for different WMAP CMB maps for  $n_{\text{side}} = 128$ .